

An efficient high-current circuit for fast radio-frequency spectroscopy in cold atomic gases

F. Scazza,^{1,2,a)} G. Del Pace,^{1,2,3} L. Pieri,⁴ R. Concas,^{1,5} W. J. Kwon,^{1,2} and G. Roati^{1,2}

¹⁾European Laboratory for Nonlinear Spectroscopy (LENS), 50019 Sesto Fiorentino, Italy

²⁾Istituto Nazionale di Ottica (CNR-INO), 50019 Sesto Fiorentino, Italy

³⁾Dipartimento di Fisica e Astronomia, Università degli Studi di Firenze, 50019 Sesto Fiorentino, Italy

⁴⁾Radioteknos, 50142 Firenze, Italy

⁵⁾Istituto Italiano di Ricerca Metrologica (INRiM), 10135 Torino, Italy

(Dated: 27 April 2021)

We design and implement an efficient high-current radio-frequency (RF) circuit, enabling fast and coherent coupling between magnetic levels in cold alkali atomic samples. It is based on a compact shape-optimized coil that maximizes the RF field coupling with the atomic magnetic dipole, and on coaxial transmission-line transformers that step up the field-generating current flowing in the coil to about 8 A for 100 W of RF power. The system is robust and versatile, as it generates a large RF field without compromising on the available optical access, and its central resonant frequency can be adjusted *in situ*. Our approach provides a cost-effective, reliable solution, featuring a low level of interference with surrounding electronic equipment thanks to its symmetric layout. We test the circuit performance using a maximum RF power of 80 W at a frequency around 82 MHz, which corresponds to a measured Rabi frequency $\Omega_R/2\pi \simeq 18.5$ kHz, i.e. a π -pulse duration of about 27 μ s, between two of the lowest states of ^6Li at an offset magnetic field of 770 G. Our solution can be readily adapted to other atomic species and vacuum chamber designs, in view of increasing modularity of ultracold atom experiments.

I. OVERVIEW

Over the past two decades, the ability to coherently manipulate the internal state of atoms and molecules has proven an essential tool in the field of precision measurements¹, as well as for the realization of ultracold synthetic matter and atomic quantum simulators of important many-body problems^{2,3}. In particular, a key experimental probe of many-body physics in ultracold atomic systems is radio-frequency (RF) spectroscopy^{2,4}, by which an applied RF pulse is used to transfer atoms from one hyperfine state to another unoccupied state. Addressing the RF transitions that connect hyperfine sublevels with different interaction properties allows for accessing the spectral properties of elementary excitations in Fermi^{5–10} and Bose gases^{11–13}, as well as fundamental thermodynamic quantities^{14–16}. In this context, a significant demand is the implementation of strong coherent RF drives, which are especially important to precisely trigger and probe non-equilibrium many-body dynamics governed by short-range interactions^{16–20}, tuned through Feshbach resonances upon varying a static magnetic field applied to the sample.

In quantum degenerate Fermi gases, a natural time scale $\tau_F = \hbar/\varepsilon_F$ is set by the Fermi energy ε_F of the system, where \hbar is the reduced Planck constant $\hbar/2\pi$. The dynamics at short times $t \sim \tau_F$ are expected to be universal, revealing the emergence of elementary excitations in real time^{18,20}, and serving as a valuable benchmark for many-body theories^{21,22}. In order to experimentally investigate such *ultrafast* dynamics in ultracold Fermi gases, it is necessary to control the spin state of the atoms over time scales on the order of τ_F , whose typical values range between 5 μ s and 50 μ s depending on the experimental sample density and atomic mass. The experimental time resolution in controlling the atomic spin state is set by the Rabi frequency Ω_R , characterizing the strength of

the coupling between an external electro-magnetic (EM) field and the dipole moment associated with the atomic spin. For a given dipole moment, the only way to increase Ω_R is to increase the amplitude of the driving field experienced by the atoms. At the same time, it is important that the circuit generating the RF field does not perturb the sensitive electronics within the surrounding apparatus. This makes the realization of quiet and efficient RF systems a priority in cold atom laboratories. Moreover, as experimental setups become more complex, including large-aperture imaging systems and multiple laser beams, critical space constraints call for unobtrusive and versatile RF circuit designs.

Here we present the design and implementation of a flexible, compact and low-cost high-current circuit for efficiently coupling a large RF magnetic field to the spin of alkali atoms, whose transitions within the ground-state manifold typically lie in the 10 – 200 MHz range, allowing for spin manipulations with $\Omega_R \sim \varepsilon_F/\hbar$. Significant complexity results from the fact that atomic samples are trapped inside a ultra-high vacuum chamber by laser light potentials, and are subject to a strong static magnetic field B_0 produced by Feshbach electromagnets. Fulfilling all design requirements, the realized system shows an excellent electronic performance, in agreement with simulations. It has been tested in a typical application case by driving the transition between two ground-state magnetic sublevels of lithium atoms, characterized by a frequency $\nu_0 \simeq 82$ MHz. Moreover, it features a very low level of interference with nearby laboratory electronic equipment, as demonstrated by an observed static B-field fractional stability of about 10^{-5} for $B_0 \simeq 770$ G. The paper is organized as follows: in Section II, we describe our approach to the RF circuit design and its main advantages with respect to common solutions, and we present the realization of the different components of the RF circuit, namely the coil, the matching network and the transmission-line transformers; in Section III, we report on the characterization of the system performance with an ideal Fermi gas of lithium atoms; in the concluding Section, we summarize and provide some outlook.

^{a)}Author to whom correspondence should be addressed. Electronic mail: scazza@lens.unifi.it

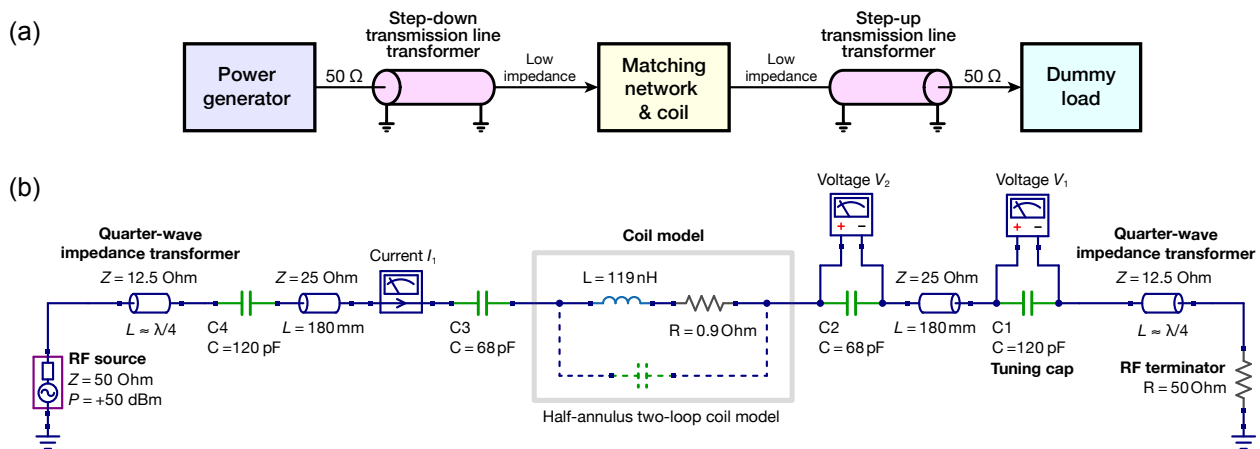


FIG. 1. Circuit concept and design. (a) A block diagram displays the five cascaded components composing the RF circuit: the generator, the step-down transformer, the matching network that compensates the coil impedance, the step-up transformer, and the $50\ \Omega$ dummy load. (b) Full layout of the RF circuit. The coil is modeled as a LR series, based on impedance measurements of the actual wire loop (see Fig. 2) inserted in a mock-up of the vacuum chamber. The step-down and step-up transformers are implemented by quarter-wave $12.5\ \Omega$ coaxial transmission lines. They respectively decrease and increase the impedance of their “secondary” sides by a factor 16. The capacitance values shown here apply to a central frequency around 83 MHz.

II. THE CIRCUIT

A. Essentials of atom spin interactions with RF fields

Energy shifts between hyperfine levels of an alkali atom depend on the applied static magnetic field, which sets the quantization direction z , and within the $J = 1/2$ ground-state manifold they can be precisely computed through the Breit-Rabi formula^{23,24}. Since transitions between hyperfine levels or Zeeman sublevels are electric-dipole forbidden, they have an extremely narrow natural linewidth, notably exploited for atomic clocks. External magnetic fields interact with the atom only through the magnetic dipolar interaction^{23,24}. In the case of ground-state Zeeman sublevels, the energy splittings for typical B_0 values correspond to RF frequencies ν_0 in the so-called very high frequency (VHF) range, roughly between 10 and 100 MHz, making RF magnetic fields the simplest method to couple different levels with one another.

Let us consider both static and RF magnetic fields that are spatially homogeneous over the scale of the atomic sample, and that the RF field is linearly polarized. We may define the static offset field as $\mathbf{B}_0 = B_0 \mathbf{e}_z$, and focus on a pair of adjacent magnetic sublevels, split by an energy $\hbar\omega_0$ associated with B_0 . These realize an effective atomic spin-1/2 system, as they coincide with the eigenstates $|m\rangle$ of the spin projection S_z along the quantization axis²⁵. The interaction of an atomic spin \mathbf{S} with a RF magnetic field $\mathbf{B}_{\text{RF}}(t) = B_{\text{RF}} \cos(\omega t + \varphi) \hat{\mathbf{e}}$ is given by $V_{\text{RF}} = \mu B_{\text{RF}} \cos(\omega t + \varphi) \mathbf{S} \cdot \hat{\mathbf{e}}$, where μ is the magnetic moment of the atomic spin²³, φ is the field phase offset, and $\hat{\mathbf{e}}$ is the RF B-field polarization unit vector. In order to couple the two $|m\rangle$ -levels with one another, the RF field polarization must have non-zero projection in the $x - y$ plane, and its frequency must be close to resonance^{23,24}, i.e. $\omega = 2\pi\nu_0$. This is the principle behind the phenomenon of nuclear magnetic resonance (NMR). Taking now $\hat{\mathbf{e}} = \mathbf{e}_y$ to maximize the coupling V_{RF} , we can define the Rabi frequency $\Omega_R = \mu B_{\text{RF}} / (2\hbar)$, characterizing the oscillation of populations between the two

atomic levels^{23,26}. The coupling strength of the RF field with an atomic spin is therefore proportional to its magnetic moment, which is fixed by the atomic isotope and the static offset field, and to the amplitude of the RF field component orthogonal to the quantization axis. The main objective of our design is maximizing the latter quantity for a given set of spatial constraints.

B. Design constraints

Atomic physics experiments require a RF B-field having the largest feasible amplitude within the sub-mm region of space occupied by the atomic sample. In many setups, atoms are however shielded inside a metallic vacuum chamber, which has only a few optical apertures. A pair of reentrant glass viewports located at cm-distance from the atoms is often included, to grant large optical access for laser beams and high-resolution imaging optics, representing also the best location where to place a RF field applicator. The RF frequency range of atomic hyperfine transitions, e.g. $\nu_0 \approx 80$ MHz for the ground-state transitions of lithium atoms, combined with the typical dimensions of the viewports and their distance from the sample, determine working conditions characteristic of magneto-quasistatic fields²⁷. In our apparatus, the reentrant viewports have a diameter of about 60 mm and their outer glass surfaces are situated at a distance of 20 mm from the sample – to be compared with RF wavelengths of at least few meters. The standard emitter to generate such quasistatic field at the near-field location of the atomic sample consists of a small coil of conductive wire. The amplitude B_{RF} in the near-field is proportional to the current flowing in such inductive loop²⁷, which must be placed as close as possible to the sample, considering that the field strength of a magnetic dipole decays with the cubed distance.

A possible strategy to minimize the distance between the RF coil and the sample, and to optimally orient the generated B-field polarization $\mathbf{B}_{\text{RF}} \perp \mathbf{B}_0$, is to accommodate the coil inside the vacuum chamber. This solution has recently become somewhat more common, but must obviously be planned

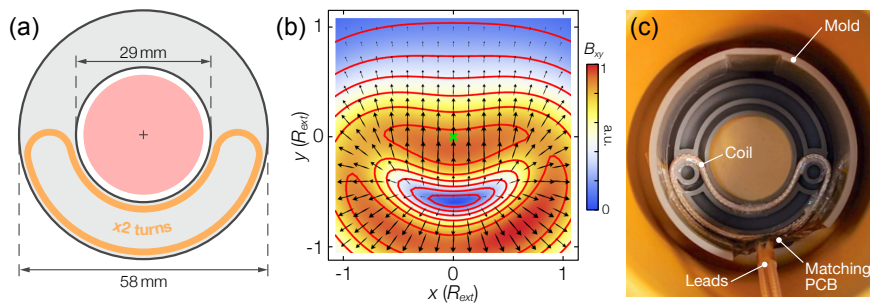


FIG. 2. Coil design and realization. (a) The coil is formed by two turns of a half-annulus shaped coaxial wire loop (orange line), with an external radius $R_{\text{ext}} \simeq 29$ mm. A clear optical aperture of 29 mm diameter, centered on the viewport remains available, used e.g. to shine a 25.4 mm-diameter beam on the atoms (pink circle). (b) Calculated B-field polarization pattern in the atomic plane at $z \simeq 20$ mm: the in-plane component B_{xy} is maximum and fairly homogeneous around the sample location $x, y = 0$ (green cross). (c) The coil has been realized using coaxial RG316 cable, and is held in shape by a 3D-printed supporting mold (gray plastic cylinder with grooves). The two lead cables visible in the bottom part of the picture connect to the coil through two capacitors C2 and C3 soldered to a cm-sized PCB [see Fig. 4(a)]. Measurements of the coil impedance are performed for simulation purposes, surrounding it with a metallic cylinder to emulate the EM environment within the re-entrant viewport.

ahead of constructing the apparatus. Further, it presents issues with flexibility and tunability, as well as risks of feedthrough and vacuum pressure failures²⁸, due to difficult heat management via the vacuum electrical feedthroughs. Therefore, we rather consider a wire loop with a diameter of few centimeters placed just outside the chamber within one of the reentrant viewports. At the center of the chamber, this will generate only a B-field, the E-field being negligible²⁹ (and unnecessary). Essentially, the coil transforms the current flowing in it into a B-field, hence in the ideal case no energy is dissipated, the only necessary entity being the current itself. Practically, some power is dissipated in conductive parts of the vacuum chamber surrounding the coil, acting as short-circuited loops, and in all resistive elements within the coil circuit placed between the generator and the coil.

C. Circuit concept and design

A common approach for maximizing the B-field is to maximize the power transfer from the RF generator towards the coil via impedance matching, by interposing a suitable network of elements between the generator and the coil^{28,30,31}. However, a coil with such small dimensions has a tiny radiation resistance of a few tens of $\text{m}\Omega$ at most for VHF frequencies, much smaller than its own loss resistance on the order of 1Ω , and negligible with respect to the 50Ω output impedance of the generator. Matching the impedance of the generator is thus practically infeasible, potentially leading to damage of the generator, unless one resorts to resistive elements which limit the transmitted current. Since the B-field hinges on the current, this approach increases the required amplifier output and it is not scalable to achieve a large B_{RF} . Moreover, widely different loads entail very high currents and voltages across the LC elements of the interposed matching network, leading to power losses³². It is also important to note that, in the absence of intended resistive loads, matching the circuit impedance to the 50Ω of the generator effectively means to transfer the RF power to the resistive losses of the coil and matching network. As a consequence, this approach eventually leads to the destruction of the matching network whenever the RF generator is turned on at sufficiently high power for a time exceeding a few milliseconds, because LC elements are

not intended for efficient dissipation. Finally, since the matching network must be placed at the location of the coil inside the reentrant viewport in order to avoid that the feedline becomes part of emitter, it is highly impractical to adjust the resonant frequency of the circuit *in situ*, as this location is usually inaccessible.

Rather than attempting to match the field-emitter to the 50Ω output impedance of the generator, we follow a different approach aimed essentially at maximizing the field-generating current in the coil³³. The basic underlying idea is to dissipate the RF power into an impedance-matched dummy load, and to interpose the coil between the generator and the load, such that the high current flowing to the load flows entirely through it, as part of a low-impedance transmission line. This concept has the additional benefit of facilitating a symmetric circuit design, which prevents undesired common-mode currents flowing on the feedline. Further, with a required generator power on the order of 100 W, our design has advantages in terms of generator cost, laboratory compatibility and reduction of the thermal stress of the entire system.

The main blocks are illustrated in Fig. 1(a), where we can see five cascaded elements: (i) RF generator with an output impedance of 50Ω ; (ii) a step-down transformer towards a lower impedance to raise the current in its “secondary” side³⁴; (iii) a matching network that compensates the self-inductance of the coil; (iv) a step-up transformer to match a load with 50Ω impedance; (v) a 50Ω dummy load that receives and dissipates the majority of the generator power. As seen from the generator, the load has a 50Ω impedance. As we will describe in the following, our design realizes the following relevant goals: (a) achieving a large RF coupling Ω_R with the atomic spin for the given available generator power; (b) allowing simple adjustment of the central frequency by a single component situated sufficiently far from coil, and wide bandwidth so to require minor tuning; (c) realizing non-critical matching and stable operation over time under temperature or mechanical deformations; (d) good mechanical and electrical robustness; (e) Electromagnetic compatibility (EMC) compliance to avoid as much as possible RF dispersion in the laboratory³⁵, causing undesired interference effects such as audio rectification³⁶.

D. The coil

A high B-field can be obtained with a coil consisting of several turns, but the self-inductance rises with the square of the number of turns. High values of the self-inductance yield a reactance that is difficult to compensate. In addition, as described previously, the generated field must be polarized orthogonally to the atom quantization axis z , i.e. $\mathbf{B}_{\text{RF}} \perp \mathbf{B}_0$. Since \mathbf{B}_0 is produced by strong electromagnets also installed in the reentrant viewports, z is directed to the viewport surface. We have considered various three-dimensional loop shapes, fulfilling the constraint of preserving a large optical access to the viewport, ranging from tilted ellipses to off-centered asymmetric profiles. The best trade-off was found with a two-turn loop shaped as a half-annulus, as depicted in Fig. 2(a), improving upon previously reported bean-shaped loops^{31,37}. This planar coil geometry maximizes the field component orthogonal to e_z [see Fig. 2(b)] for the fixed minimum distance between the atoms location and the coil. Moreover, as the generated field is almost fully polarized in the x - y plane, it is nearly homogeneous over several millimeters around the atomic sample location, rendering the design robust to manufacturing imperfections. The coil has been realized using the same coaxial cable used for transmission-line transformers (see next paragraph). Using coaxial cable is not essential, as RF currents flow only on the braid and the central conductor is inactive, but it simplifies the construction and makes it reliable even for high powers.

E. Circuit implementation and simulation

The circuit is implemented according to the schematic in Fig. 1(b). Figure 3 shows a simulation of the whole circuit carried out with the Qucs software³⁸, which guided the choice of the actual components and parameters. To match the impedance from 50Ω (generator) to a lower value suitable to increase the current in the coil, a $\lambda/4$ transmission-line transformer³² has been used. The relationship between the characteristic impedance of the line Z_0 , and the impedances

seen at the input side Z_{in} and output side Z_{out} of the transformer is given by:

$$Z_{\text{out}} = \frac{Z_0^2}{Z_{\text{in}}} \quad (1)$$

Thus, to have a large impedance variation towards lower values, it is necessary to have low-impedance transmission lines. Lines with characteristic impedance between 10Ω and 75Ω are available, but for simplicity we have chosen to use only 25Ω coaxial cables. Using two 25Ω coaxial cables in parallel (or equivalently four 50Ω cables), has approximately the same effect of using a single 12.5Ω cable, with the added advantage of power sharing between different cables, such that small ones can be used. With this choice, the impedance seen after the transformer towards generator is ideally 3.125Ω , namely 16 times lower than the original value such that the current is 4 times higher. More dramatic impedance reductions are feasible by adding further cables in parallel, but parasitic resistances of a few $100 \text{ m}\Omega$ of the coil (skin effect) and solder connections become a limiting factor.

The matching network, which includes series capacitors and 25Ω coaxial cables and incorporates the coil, serves to cancel the inductive reactance of the coil itself. The 25Ω cable sections also facilitate the installation and the manual capacitance tuning in the intricate environment close to the experimental chamber. After the last (tunable) capacitor C1, another $\lambda/4$ transformer rises again the impedance from 3.125Ω to 50Ω , matching that of the dummy load. As can be seen from simulations shown in Fig. 3, in addition to a good matching, the current I_1 is greatly increased compared to what would be obtained using simply a 50Ω generator giving 100 W , over a relatively wide frequency bandwidth of about 10 MHz . Other graphs show the voltages V_1 and V_2 across capacitors C1 and C2, which are well below the maximum working voltage of ceramic capacitors such as the ATC 100B series.

In our simulations, the coil has been modeled as a LR series,

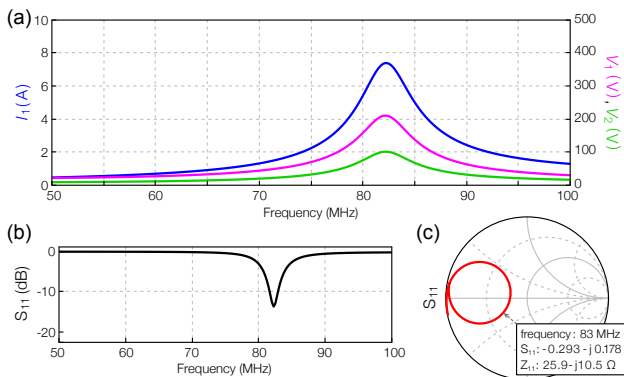


FIG. 3. Circuit simulation results. (a) The current I_1 in the coil (blue), and the voltages V_1 (magenta) and V_2 (green) across the matching capacitors C1 and C2, respectively, are displayed. (b)-(c) The modulus and Smith chart of the circuit S_{11} parameter are shown, quantifying the power reflected to the generator.

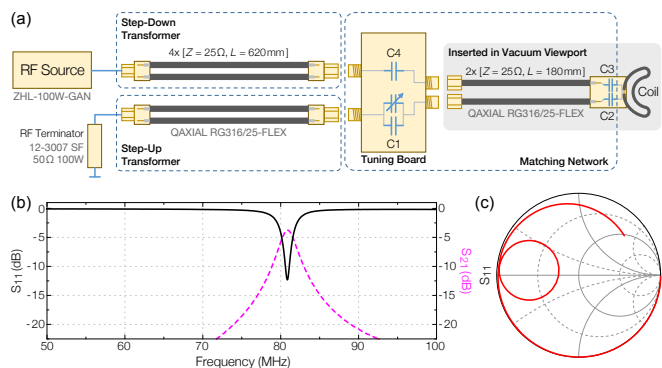


FIG. 4. Circuit realization and *in situ* measurements. (a) Fixed capacitors are ATC-100B series, while the tuning capacitance in C1 is realized with a Johanson MAV05D30. Capacitors C2 and C3 are hosted by a cm-sized PCB mounted vertically next to the coil within the plastic housing [see Fig. 2(c)]. Conversely, capacitors C1 and C4 are soldered on a dedicated PCB, which is housed and fixed to an optical breadboard outside the reentrant viewport. (b)-(c) The S_{11} parameter measured with a VNA are found in good agreement with simulations [see Fig. 3(b)-(c)]. The S_{21} parameter quantifies the power reaching the final 50Ω load, and equals about -3 dB at the resonance (here tuned to 81 MHz).

whose values are based on vector impedance measurements of the actual coil build [see Fig. 2(c)]. Given the low RF frequencies involved and the small dimensions, no parasitic resonance was observed, so the model turned out to be particularly simple – no parallel capacitance is included. As described in the following paragraphs, measurements and simulations are in close agreement.

F. Realization

Figure 4 shows a sketch of the realized circuit. We opted to use add an extra transmission-line section of 180 mm length, to reach the vacuum viewport of the experiment while keeping the tuning capacitor C1 at reach. The system is built using a $Z_0 = 25 \Omega$ coaxial cable (QAXIAL RG316/25-FLEX) with non-magnetic conductors and high-power handling of ~ 500 W at 80 MHz, and high-voltage porcelain multilayer SMD capacitors from American Technical Ceramics (ATC 100B series, non-magnetic). All ATC capacitors are able to withstand 1 kV. To hold the coil in shape, a plastic support has been realized with a 3D printer, increasing the robustness of the system and facilitating the insertion of the coil in the vacuum viewport mechanic clearance. The step-down and step-up transformers are realized using two couples of 620 mm-long coaxial sections, corresponding to $\lambda/4$ segments at 80 MHz. The matching network includes: (i) Capacitors C2 and C3, used to create a matching between the loop and the line; (ii) A pair of coaxial cables with characteristic impedance $Z_0 = 25 \Omega$ which link the C2/C3 board to the network matching (and tuning) board; (iii) Capacitors C1 and C4, realized with 2 fixed capacitors and a tunable trimmer capacitor, necessary for finely tuning the resonance frequency. The latter is implemented by an air dielectric trimmer capacitor from Johanson Technology, with a voltage rating of 500 V, a capacitance range of 1 pF – 30 pF and a Q-factor > 800 at 100 MHz.

III. CIRCUIT PERFORMANCE

A. Electrical network measurements

The measurement phase started with the characterization of the coil impedance to determine the actual L and R parameters to input in the circuit model. The matching network has been designed, realized and tested on the workbench. Subsequently, the coil has been inserted in the viewport and the complete system tested *in situ*. Illustrative measurements performed with a vector network analyzer (VNA) are shown in Fig. 4(b)-(c). The circuit resonant frequency can be shifted over a range of about 2 MHz varying the value of C4 by 30 pF without visibly reducing the impedance matching.

B. Testing the system on atomic samples

We have tested the system in our experiment with ultracold degenerate gases of fermionic lithium atoms^{2,19}. We have addressed the transition between the second-lowest and third-lowest magnetic sublevels of ${}^6\text{Li}$ ground state, usually labeled $|2\rangle$ and $|3\rangle$, respectively. In the experiment, offset fields in the range $B_0 \simeq 570$ G – 900 G are used², covering the position of two broad Feshbach resonances at 690 G and 832 G

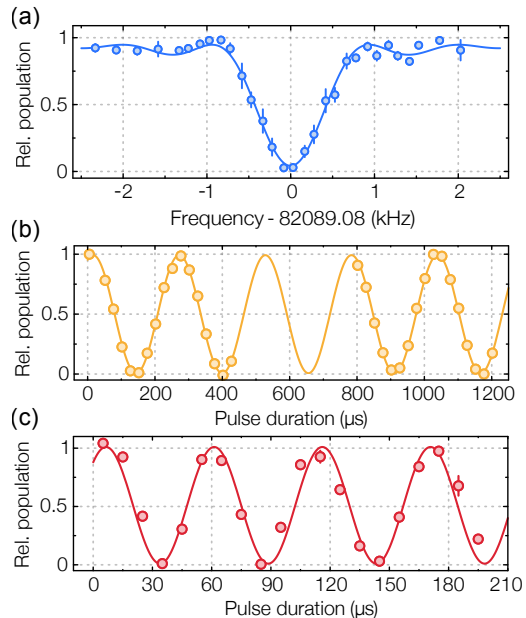


FIG. 5. System performance measured with an ideal Fermi gas of ${}^6\text{Li}$ atoms at $B_0 \simeq 770$ G. On the vertical axis, the relative population denotes the number of atoms in state $|2\rangle$ normalized to the total atom number. (a) Spectroscopy of the $|2\rangle \leftrightarrow |3\rangle$ transition. The solid line is a fit of the data with the expected sinc-function lineshape, yielding a resonance frequency $\nu_0 = 82.08908(1)$ MHz and a Rabi frequency $\Omega_R/2\pi = 410(16)$ Hz. (b)-(c) Rabi oscillations at the resonance between states $|2\rangle$ and $|3\rangle$ for RF generator powers of about 3.5 W (yellow) and 80 W (red). Solid lines are sinusoidal fits to the data, yielding Rabi frequencies $\Omega_R/2\pi = 3.909(4)$ kHz and $\Omega_R/2\pi = 18.25(23)$ kHz, respectively.

between states $|2\rangle$ and $|3\rangle$, and the lowest hyperfine level $|1\rangle$. For such B_0 values, nuclear and electron spins of the atom are largely decoupled²³, and the spin system formed by states $|2\rangle$ and $|3\rangle$ has a low magnetic moment $|\mu|/h \lesssim 10$ kHz/G (still about 10 times larger than the nuclear magnetic moment $\mu_N \simeq \mu_B/1836$, with $\mu_B/h \simeq 1.4$ MHz/G).

A spectroscopic measurement of the $|2\rangle \leftrightarrow |3\rangle$ transition in an ideal (spin-polarized) degenerate Fermi gas at $B_0 \simeq 770$ G is displayed in Fig. 5(a). A sinc-shaped line centered around 82 MHz is observed, associated with the 1 ms-long square pulse at 50 mW of RF power, used for the spectroscopic transfer shown here. A spectral stability below 100 Hz is observed during several minutes necessary for a full spectroscopic measurement, corresponding to an offset B-field stability below 10 mG, or a fractional stability around 10^{-5} .

In order to benchmark the performance of our RF system at high power, we have performed Rabi oscillation measurements at the measured resonance of the $|2\rangle \leftrightarrow |3\rangle$ transition. Illustrative results are displayed in Fig. 5(b)-(c), where a coherent sinusoidal evolution of the state populations is visible for two different driving powers. The intrinsic lifetime of the hyperfine states is much longer than the typical measurement time scales, guaranteeing that visible damping originates only from dephasing from magnetic field fluctuations. Since no measurable damping is observed over the time scales of the evolution, we conclude that our RF setup does not significantly influence the surrounding electronic equipment, used to actively stabilize the value of B_0 (comprised of current transducers, analog PID loops, and DC regulated power sup-

plies). Extracting the Rabi frequency with a sinusoidal fit to the data, we find $\Omega_R/2\pi \simeq 18.25$ kHz for a driving power of about 80 W. This corresponds to a π -pulse duration of 27.5 μ s, which is on the order of the Fermi time $\tau_F \simeq 30$ μ s in our degenerate Fermi gas, fulfilling our main design goal³⁹.

IV. CONCLUSIONS

In this paper we have described an alternative approach to the generation of quasistatic RF magnetic fields for atomic physics experiments. This provides an efficient, low-cost and uncomplicated solution to achieve large coupling strength with atomic spins, without introducing detrimental disturbances or reliability issues. In principle, the realized circuit is able to withstand short pulses with larger RF power $P > 100$ W, further increasing the maximum Rabi frequency. Our design can be readily adapted to address relevant transitions between adjacent magnetic sublevels of other fermionic and bosonic alkali atomic species, such as K, Rb, Na or Cs, with frequencies lying in the 10–200 MHz range, and to different optical apertures or positioning constraints – possibly also for in-vacuum coils, where tilted or deformed circular loops may be considered. For frequencies exceeding 200 MHz, the RF coil features a typical radiation resistance around 1 Ω , and thus its behavior crosses over to that of a small-loop antenna⁴⁰, for which the radiated power becomes significant. We believe our system may constitute a standard solution for RF field coupling to alkali atom spins in forthcoming experimental setups, where large optical access and modularity have nowadays become a must.

ACKNOWLEDGMENTS

We thank Andreas Trenkwalder, Michael Jag, Alessio Ciamei, Matteo Zaccanti, Marco De Pas, and the LENS electronic workshop for useful discussions, Caterina Credi for help with 3D printing, and Massimo Inguscio for constant support. This work was supported by the Italian Ministry of University and Research under the PRIN2017 project CEN-TraL, and European Union’s Horizon 2020 research and innovation programme under the Qombs project FET Flagship on Quantum Technologies GA no. 820419, and Marie Skłodowska-Curie GA no. 843303.

DATA AVAILABILITY STATEMENT

The data that support the findings of this study are available from the corresponding author upon reasonable request.

REFERENCES

- ¹M. Inguscio and L. Fallani, *Atomic physics: precise measurements and ultracold matter* (Oxford University Press, 2013).
- ²W. Ketterle and M. Zwierlein, *Proceedings of the International School of Physics “Enrico Fermi,” Course CLXIV, Varenna, 20–30 June 2006* (2008).
- ³M. Inguscio, W. Ketterle, S. Stringari, and G. Roati, eds., *Proceedings of the International School of Physics “Enrico Fermi” – Course 191 “Quantum Matter at Ultralow Temperatures”* (IOS Press, Amsterdam; SIF, Bologna, 2016).
- ⁴P. Törmä, *Physics of ultracold Fermi gases revealed by spectroscopies*, Phys. Scripta **91**, 043006 (2016).
- ⁵C. Chin, M. Bartenstein, A. Altmeyer, S. Riedl, S. Jochim, J. H. Denschlag, and R. Grimm, *Observation of the Pairing Gap in a Strongly Interacting Fermi Gas*, Science **305**, 1128 (2004).
- ⁶J. T. Stewart, J. P. Gaebler, and D. S. Jin, *Using photoemission spectroscopy to probe a strongly interacting Fermi gas*, Nature **454**, 744 (2008).
- ⁷A. Schirotzek, C.-H. Wu, A. Sommer, and M. W. Zwierlein, *Observation of Fermi Polarons in a Tunable Fermi Liquid of Ultracold Atoms*, Phys. Rev. Lett. **102**, 230402 (2009).
- ⁸C. Kohstall, M. Zaccanti, M. Jag, A. Trenkwalder, P. Massignan, G. M. Bruun, F. Schreck, and R. Grimm, *Metastability and coherence of repulsive polarons in a strongly interacting Fermi mixture*, Nature **485**, 615 (2012).
- ⁹M. Koschorreck, D. Pertot, E. Vogt, B. Fröhlich, M. Feld, and M. Köhl, *Attractive and repulsive Fermi polarons in two dimensions*, Nature **485**, 619 (2012).
- ¹⁰F. Scazza, G. Valtolina, P. Massignan, A. Recati, A. Amico, A. Burchianti, C. Fort, M. Inguscio, M. Zaccanti, and G. Roati, *Repulsive Fermi Polarons in a Resonant Mixture of Ultracold ⁶Li Atoms*, Phys. Rev. Lett. **118**, 083602 (2017).
- ¹¹M.-G. Hu, M. J. Van de Graaff, D. Kedar, J. P. Corson, E. A. Cornell, and D. S. Jin, *Bose Polarons in the Strongly Interacting Regime*, Phys. Rev. Lett. **117**, 055301 (2016).
- ¹²N. B. Jørgensen, L. Wacker, K. T. Skalmstang, M. M. Parish, J. Levinsen, R. S. Christensen, G. M. Bruun, and J. J. Arlt, *Observation of Attractive and Repulsive Polarons in a Bose-Einstein Condensate*, Phys. Rev. Lett. **117**, 055302 (2016).
- ¹³Z. Z. Yan, Y. Ni, C. Robens, and M. W. Zwierlein, *Bose polarons near quantum criticality*, Science **368**, 190 (2020).
- ¹⁴Y. Sagi, T. E. Drake, R. Paudel, and D. S. Jin, *Measurement of the Homogeneous Contact of a Unitary Fermi Gas*, Phys. Rev. Lett. **109**, 220402 (2012).
- ¹⁵B. Mukherjee, P. B. Patel, Z. Yan, R. J. Fletcher, J. Struck, and M. W. Zwierlein, *Spectral Response and Contact of the Unitary Fermi Gas*, Phys. Rev. Lett. **122**, 203402 (2019).
- ¹⁶R. J. Fletcher, R. Lopes, J. Man, N. Navon, R. P. Smith, M. W. Zwierlein, and Z. Hadzibabic, *Two- and three-body contacts in the unitary Bose gas*, Science **355**, 377 (2017).
- ¹⁷A. B. Bardon, S. Beattie, C. Luciuk, W. Cairncross, D. Fine, N. S. Cheng, G. J. A. Edge, E. Taylor, S. Zhang, S. Trotzky, and J. H. Thywissen, *Transverse Demagnetization Dynamics of a Unitary Fermi Gas*, Science **344**, 722 (2014).
- ¹⁸M. Cetina, M. Jag, R. S. Lous, I. Fritsche, J. T. M. Walraven, R. Grimm, J. Levinsen, M. M. Parish, R. Schmidt, M. Knap, and E. Demler, *Ultrafast many-body interferometry of impurities coupled to a Fermi sea*, Science **354**, 96 (2016).
- ¹⁹A. Amico, F. Scazza, G. Valtolina, P. E. S. Tavares, W. Ketterle, M. Inguscio, G. Roati, and M. Zaccanti, *Time-Resolved Observation of Competing Attractive and Repulsive Short-Range Correlations in Strongly Interacting Fermi Gases*, Phys. Rev. Lett. **121**, 253602 (2018).
- ²⁰M. G. Skou, T. G. Skov, N. B. Jørgensen, K. K. Nielsen, A. Camacho-Guardian, T. Pohl, G. M. Bruun, and J. J. Arlt, *Non-equilibrium quantum dynamics and formation of the Bose polaron*, Nat. Phys. (2021), 10.1038/s41567-021-01184-5.
- ²¹R. Schmidt, M. Knap, D. A. Ivanov, J.-S. You, M. Cetina, and E. Demler, *Universal many-body response of heavy impurities coupled to a Fermi sea: A review of recent progress*, Rep. Prog. Phys. **81**, 024401 (2018).
- ²²H. S. Adlong, W. E. Liu, F. Scazza, M. Zaccanti, N. D. Oppong, S. Fölling, M. M. Parish, and J. Levinsen, *Quasiparticle Lifetime of the Repulsive Fermi Polaron*, Phys. Rev. Lett. **125**, 133401 (2020).
- ²³D. A. Steck, *Quantum and atom optics* (revision 0.13.4, September 24, 2020).
- ²⁴B. H. Bransden and C. J. Joachain, *Physics of atoms and molecules* (Pearson Education, 2003).
- ²⁵While the considered spin S typically maps to the total angular momentum F of the hyperfine atomic state, in the limit of large magnetic fields B_0 it approaches the nuclear spin I , which decouples from the electronic shell²⁴.
- ²⁶H. Perrin and B. M. Garraway, *Trapping Atoms With Radio Frequency Adiabatic Potentials*, edited by E. Arimondo, C. C. Lin, and S. F. Yelin, Adv. At. Mol. Opt. Phys., Vol. 66 (Academic Press, 2017).
- ²⁷H. A. Haus and J. R. Melcher, *Electromagnetic fields and energy*, Vol. 107 (Prentice Hall, Englewood Cliffs, NJ, 1989).
- ²⁸Z. A. Geiger, *An apparatus for dynamical quantum emulation using ultracold lithium*, Ph.D. thesis, University of California Santa Barbara (2018).

- ²⁹In such near-field quasistatic condition, it is indeed inappropriate to refer to the emitter as an “antenna”, since the propagating electromagnetic radiation is irrelevant, and we will henceforth simply refer to it as the “coil”.
- ³⁰A. N. Wenz, *Few-body physics in a three-component Fermi gas*, Master’s thesis, University of Heidelberg (2009).
- ³¹D. Mitra, *Exploring attractively interacting fermions in 2D using a quantum gas microscope*, Ph.D. thesis, University of Princeton (2018).
- ³²R. E. Collin, *Foundations for microwave engineering* (John Wiley & Sons, 2007).
- ³³D. S. Barker, A. Restelli, J. A. Fedchak, J. Scherschligt, and S. Eckel, *A radiofrequency voltage-controlled current source for quantum spin manipulation*, *Rev. Sci. Instr.* **91**, 104708 (2020).
- ³⁴Although the wording “primary” and “secondary” is imprecise for the coaxial transmission-line transformers that are implemented, these terms are used to clarify the concept.
- ³⁵J. Brown, *A Ham’s Guide to RFI, Ferrites, Baluns, and Audio Interfacing* (Self-published, 2007).
- ³⁶The most fundamental cause of RF interference (RFI) is the fact that the wirings of laboratory equipment act as antennas. Besides proper shielding of equipment, ferrite chokes (Fair-Rite #43 or #31 materials) can be an effective tool to eliminate inductive RF field coupling into wires³⁵.
- ³⁷T. Lompe, *Efimov Physics in a three-component Fermi gas*, Ph.D. thesis, University of Heidelberg (2011).
- ³⁸Available under GPL license at <http://qucs.sourceforge.net>.
- ³⁹For comparison, a previously employed circuit, based on direct impedance matching of a tilted, elliptic small loop via a capacitor network, yielded a Rabi frequency around $\Omega_R/2\pi \simeq 4.5$ kHz by applying 80 W of RF power within the same experimental setup.
- ⁴⁰J. Kraus, *Antennas* (McGraw-Hill, 1988).